Vertically Polarized, High Performance, Electrically Small Monopole Filtennas

Ming-Chun Tang, Piao Guo, Dajiang Li, Kun-Zhi Hu, Mei Li, and Richard W. Ziolkowski

***Abstract* — Vertically polarized, omnidirectional and endfire radiating, bandwidth-enhanced, high efficiency, electrically small monopole filtennas are developed. Both designs are attained by organically combining a coax-fed top-hat loaded monopole with two hybrid quarter-wavelength open-end stubs and a shorting post. The hybrid stubs serve two functions. They produce two radiation nulls at both the lower and upper band-edges to sharpen the roll-off rate. Moreover, they facilitate the appearance of an additional resonance without affecting the original resonant mode. The shorting post is introduced to engineer the overlap of two resonant modes to yield an enhanced bandwidth. Prototypes of both filtennas were fabricated, assembled, and tested. The measured results are in good agreement with their simulated values, validating their efficacy. The omnidirectional filtenna has an electrically small size ($ka = 0.73$), a fractional bandwidth (FBW) of 11.3%, and a maximum realized gain of 3.01 dBi. The endfire radiating filtenna has an electrically small size ($ka = 0.93$), an operating FBW of 12.8%, and a peak realized gain of 6.09 dBi. Both filtennas exhibit a flat realized gain response and high radiation efficiencies over their entire passbands, as well as very good selectivity with high out-of-band suppression levels.

***Index Terms*—Electrically small antennas, endfire, filtennas, monopole antennas, omnidirectional, vertical polarization**

I. Introduction

Compared with horizontally polarized (HP) antennas, vertically polarized (VP) ones hold the performance advantage that their path losses are inherently much smaller when an electromagnetic wave propagates along a lossy medium such as the earth or realistic ground planes [1]-[5]. Consequently, VP antennas have been widely applied to many practical engineering scenarios beyond the land, water and air vehicles ones, e.g., unattended ground sensor networks [6], wireless local area network (WLAN) systems [7], communications and sensing in tunnel environments [8], and on-road radio frequency identification (RFID) enabled intelligent parking systems [9].

Filtennas, i.e., the intrinsic combinations of antennas and filters, have recently been championed for their compact size advantages. In particular, VP filtennas would have an additional desirable advantage

over simpler VP antenna-only designs because they would integrate and provide an application with both radiating and filtering functions. Nevertheless, only one VP filtenna has been reported to date [10]. It was a VP dielectric resonator antenna (DRA) realized by loading the interior of its dielectric resonator with a ring slot and four shorting pins and by feeding it with a hybrid structure. It exhibited filter-like frequency responses in both its reflection coefficient and realized gain performance. Moreover, it provided a wide 52.8% fractional bandwidth (FBW) and a flat gain of ~0.84 dBi within that passband. However, it had an inevitable high profile and its operating properties further contributed to it being electrically large in size, making it unsuitable for space-limited wireless platforms.

In this Communication, two electrically small, VP monopole filtennas are developed. One is an omnidirectional radiating system and the other is an endfire radiating version. Both designs are attained by organically combining a coax-fed top-hat loaded monopole with two hybrid quarter-wavelength open-end stubs and a shorting post. The hybrid stubs and shorting post facilitate an enhanced bandwidth and improved frequency selectivity without any influence on the original radiation behavior of the monopole. Recall that an electrically small antenna (ESA) has $ka_{radiator} < 1$, where $a_{radiator}$ is the radius of the smallest sphere that completely encloses the entire radiator and $k = 2\pi/\lambda_L = 2\pi f_L/c$ is the free-space wavenumber corresponding to the lower bound of the operating frequency range, f_L.

Two optimized prototypes were fabricated and tested to verify their predicted performance. The omnidirectional one was electrically small with $ka_{radiator} = 0.73$, and it operated in the frequency range from 1.76 to 1.97 GHz, a 11.3% FBW, with an average realized gain ~2.76 dBi. The endfire one was also electrically small with $ka_{radiator} = 0.93$. It operated in the frequency range from 1.9 to 2.16 GHz, a 12.8% FBW, with an average realized gain of ~5.38 dBi. The measured results were in good agreement with their simulated values.

II. Omnidirectional, Electrically Small, VP, Top-Hat Loaded Monopole-Based Filtenna

The omnidirectional, electrically small, VP, top-hat loaded monopole-based filtenna configuration is shown in Fig. 1. The corresponding optimized design parameters are detailed in Table I. As shown in Fig. 1, the antenna is composed of two substrates, two copper posts, and a metal ground plane. These substrates are Rogers RO4003, with a relative dielectric constant $\varepsilon_r = 3.55$, loss tangent *tan δ* = 0.0027, and a 0.017 mm copper cladding thickness. The upper substrate is a circular disk with a radius of 15.0 mm and a thickness of 0.813 mm. The lower substrate is also a circular disk with a larger radius, 21.0 mm, and the same thickness, 0.813 mm. A circular copper ground plane with a much larger radius, 165 mm, and a 1.0 mm thickness is placed directly under the lower substrate.

As indicated in Figs. 1(a) and 1(b), the two ends of the driven post are connected, respectively, to the bottom surface of the top hat and to the end of the inner conductor of the SMA connector. The shorting post penetrates through both substrates to connect the top-hat directly to the ground plane. Two quarter-wavelength open-end stubs with different lengths are etched on the top surface of the lower substrate. They are closely arranged in parallel with the gap distance between

them being only g = 0.2 mm. Their top arc parts are curved in opposite directions to achieve compactness. A rectangular patch on the shorter stub is $L_1 \times W_1$ in size, and a rectangular slot cut in the longer stub on the side nearest to the shorter stub is $L_2 \times W_2$ in size. These elements were integrated into the two stubs to optimize the impedance matching within the operational band. A 50 Ω SMA connector with a 0.45 mm radius inner conductor passes vertically through the lower substrate and is connected to both stubs as shown in Fig. 1(c), and its outer conductor is connected to the ground plane.
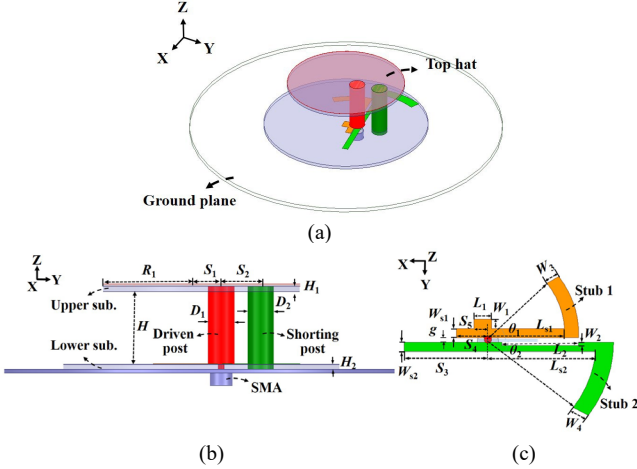

Fig. 1. The configuration of the omnidirectional, electrically small, VP, top-hat loaded monopole-based filtenna. (a) 3-D isometric view. (b) Side view. (c) Top view of the hybrid quarter-wavelength open-end stubs. Stub 1 (Stub 2) is the shorter (longer) stub.

TABLE I OPTIMIZED DESIGN PARAMETERS OF THE OMNIDIRECTIONAL, ELECTRICALLY SMALL, VP, MONOPOLE-BASED FILTENNA (IN MILLIMETERS)

S_1 =3.0	S_2 = 6.0	L_{s1} = 11	W_{s1} = 1.5	R_1 = 15.0
D_1 = 4.0	D_2 = 4.0	L_{s2} = 15.5	W_{s2} = 1.5	H = 11.3
L_1 = 2.0	W_1 = 2.5	L_2 = 11.0	W_2 = 0.5	H_1 = 0.813
W_3 = 2.0	W_4 = 2.5	S_3 = 12.0	S_4 = 4.5	H_2 = 0.813
S_5 = 2.0	g = 0.2	θ_1 = 32°	θ_2 = 30°	None

A. Operating Mechanisms

The operating mechanisms of the omnidirectional-radiating filtenna can be illustrated using five stages of the evolution of the top-hat monopole antenna and its stub and post augmentations. They are: 1) top-hat monopole; 2) top-hat monopole with a quarter-wavelength open-end stub; 3) top-hat monopole with two open-end stubs; 4) top-hat monopole with two open-end stubs and a shorting post; and 5) the optimized filtenna.

Step I, a typical top-hat monopole antenna: Ant. I radiates a VP field. The presence of the top-hat significantly decreases the monopole's profile and thus helps reduce its electrical size [11]. As illustrated in Fig. 2, there is no filtering performance.

Step II, Ant. II is Ant. I augmented with Stub 1: The shorter custom-engineered quarter-wavelength stub, Stub 1, is introduced into Ant. I. As shown in Fig. 2, a radiation null close to the upper band edge appears. Thus, the suppression level of the filter near the upper edge of the passband is greatly improved. This radiation null is generated because the shorter quarter-wavelength open-end transmission line, Stub 1, achieves a transmission zero near the passband's upper edge [12]. In particular, the quarter-wavelength frequency of Stub 1 is [12], $f_{\text{Stub 1}} = c / 4L\sqrt{\varepsilon_{re}}$, where c is the speed of light in vacuum, L is total length of the stub, and ε_{re} is the equivalent dielectric constant of the microstrip transmission line formed by the stub, substrate, and ground plane.

Step III, Ant. III is Ant. II augmented with Stub 2: In the same manner, the longer length Stub 2 introduces a radiation null near the lower edge of the passband. As presented in Fig. 2, Stub 2 is introduced in parallel with Stub 1 and its top arc is oriented in the opposite direction. Because of the loading of Ant. II with the longer Stub 2, the roll-off rate at the lower band-edge of Ant. III's passband has been greatly improved. In particular, Ant. III has two deep radiation nulls near its lower and upper passband-edges and, thus, yields a very good passband filter response. Nevertheless, the antenna has poor in-band impedance matching. Moreover, an additional resonant mode has appeared at the higher frequency, 1.84 GHz, which is quite close to the original resonance of Ant. I.

Step IV, Ant. IV is Ant. III augmented with the shorting post: The in-band impedance match is improved by introducing the vertical shorting post into Ant. III that connects the top-hat to the ground plane. The presence of the shorting post increases the resistance and reduces the reactance parts of the monopole mode's input impedance, and thus, it achieves a better impedance matching as illustrated in Fig. 2. However, to significantly improve the impedance bandwidth, the mode associated with the two stubs must be matched better. In order to address this mismatch, it was found that a rectangle slot had to be introduced into Stub 2 and Stub 1 had to be loaded with a rectangular patch. Furthermore, it was determined that by moving the monopole location on the top-hat away from its center allows one to control the relative frequency difference between the monopole and stub modes. The bandwidth is then increased by tailoring the overlap of the resonances of those two modes. Care must be exercised when optimizing the overlap because there is a tradeoff between the operational bandwidth and the level of the impedance match.

Step V, Ant. IV is optimized: Finally, the off-center design of Ant. IV was optimized to obtain Ant. V. As indicated in Fig. 2, the two in-band resonances of Ant. V attained nearly perfect impedance matching. Moreover, a flat realized gain response within the passband and sharp roll-offs at band edges was accomplished.
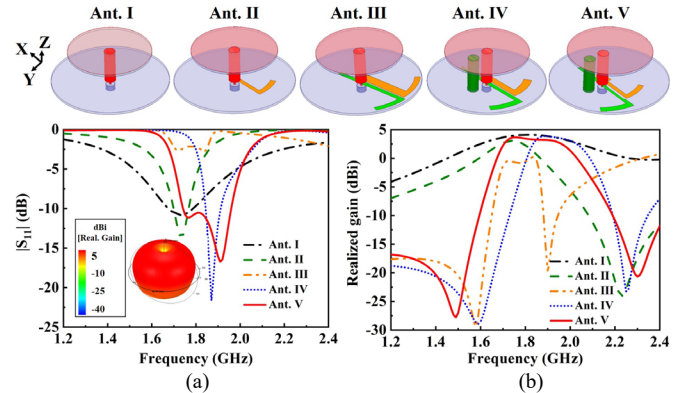

Fig. 2. The omnidirectional-radiating filtenna evolution. The configurations of all five antennas are indicated in the top row of subplots. The corresponding simulated results are indicated in the bottom subplot. (a) The reflection coefficients ($|S_{11}|$), the 3-D radiation patterns of corresponding resonant mode of the Ant. I is given in the inset. (b)The realized gain.

The resonance frequency of the mode produced by the two stubs is simply calculated [12]. Because the two quarter-wavelength stubs are connected by their common coaxial feed, they form a half-wavelength resonator. Its resonance frequency is $f_{\text{two stubs}} = c / 2L_{\text{two stubs}}\sqrt{\varepsilon_{re}}$, where $L_{\text{two stubs}}$ is the total current pathway of the resonant mode, which is illustrated below. The optimized parameters given in Table I were used to find $f_{\text{two stubs}} \sim$ 1.93 GHz, which is quite close to the simulated value, 1.92 GHz. The

–10 dB FBW is 11.9%, while it has an electrically small size, $ka_{radiator}$ = 0.72. Note that fields radiated by the currents driven on the two stubs are basically absent in their broadside direction because of their parallel orientation. Thus, a uniform, monopole-like VP realized gain pattern is dominant and stable across the entire operating band.

B. Current Distributions and Parametric Studies

The nulls in the optimized antenna's realized gain curve occur at 1.49 and 2.3 GHz. The surface current distributions on the top hat, posts and stubs at these two null frequencies are detailed in Fig. 3. As shown in Fig. 3(a), a strong current is concentrated on Stub 2 at 1.49 GHz, while that on Stub 1 is relatively weak despite their close proximity. This feature further confirms that the physical parameters of the longer Stub 2 are intimately tied to this lower null frequency. Similarly, Fig. 3(b) shows that a strong current is concentrated on Stub 1 at the upper realized gain null frequency, 2.3 GHz, while only a very weak one exists on Stub 2. Thus, the physical parameters of the shorter Stub 1 are intimately connected to this upper null frequency. The currents on the posts and top hat are quite weak at both null frequencies. Thus, the majority of the electromagnetic energy is well localized near to the stubs. Consequently, the roll-off at both passband edges is sharp, yielding a very good filter response.
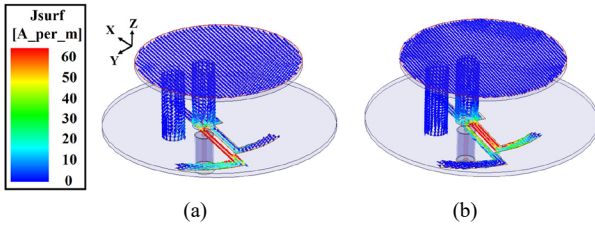

Fig. 3. Surface current distributions on the optimized filtenna at its radiation null frequencies: (a) 1.49 GHz, and (b) 2.3 GHz.

On the other hand, the surface current distributions at the in-band resonances at 1.77 and 1.92 GHz are shown in Fig. 4. At the lower resonance frequency, 1.77 GHz, the surface current on both posts are vertically oriented in the same direction. This behavior enables its VP radiated fields at that frequency. In contrast, while the currents on the posts are strong at the higher resonance frequency, 1.92 GHz, they are much weaker than those on the stubs. The currents on the stubs are in phase but are flowing in opposite directions. Thus, while they form a half-wavelength resonance, they radiate a difference field in their broadside direction, i.e., the HP radiated field components are very weak. Consequently, the system also radiates essentially a VP field at the higher resonance frequency.
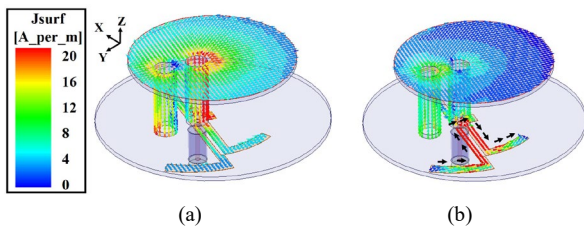

Fig. 4. Surface current distributions on the optimized filtenna at its in-band resonance frequencies: (a) 1.77 GHz, and (b) 1.92 GHz.

The influence of two key design parameters, the angles θ_1 and θ_2 that determine the lengths of the top arcs of the stubs, on the two radiation nulls was investigated parametrically. As shown in Fig. 5, when the arc angle θ_1 of Stub 1 increases from 30° to 40°, the upper-band radiation null exhibits a red-shift while the lower-band radiation null remains effectively unchanged. Similarly, when the arc angle θ_2 of Stub 2 increases from 30° to 40°, the lower radiation null

also exhibits a red-shift and the high-frequency radiation null is essentially unaffected. Therefore, the frequency positions of the two radiation nulls can be independently tuned by changing the arc lengths of the corresponding stubs.
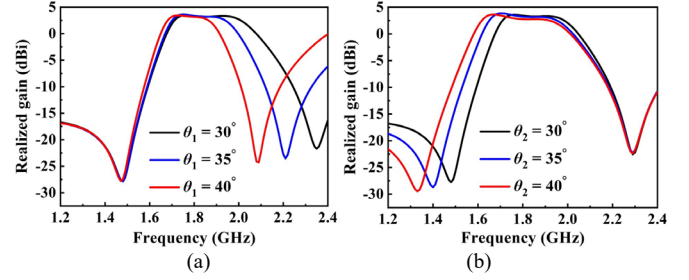

Fig. 5. Simulated peak realized gains against (a) the top bending angle of the Stub 1 θ_1 and (b) the top bending angle of the Stub 2 θ_2.

C. Measurement Results

Ant. V, the optimized omnidirectional-radiating VP filtenna, was fabricated, assembled and tested. Photographs of the prototype are shown in Fig. 6. Note in Fig. 6(b) that its large, 165 mm radius circular ground plane helps to improve the accuracy of the measurements of its VP radiation characteristics. The S-parameters were measured with an Agilent E8361A PNA vector network analyzer (VNA). Its far-field radiation performance characteristics were measured with an SG128 multi-probe antenna measurement system at the China Academy of Information and Communications Technology, Chongqing, China [13].
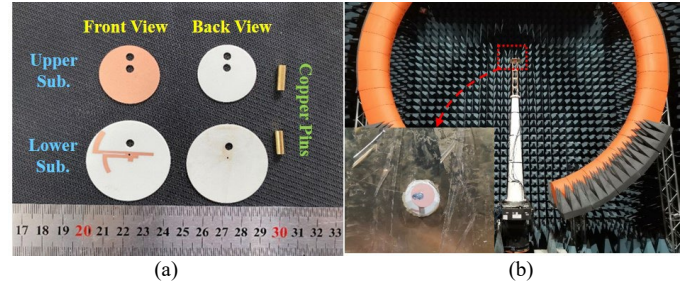

Fig. 6. Fabricated omnidirectional, electrically small, VP, top-hat loaded monopole-based filtenna. (a) Front and back views of each layer before assembly. (b) Antenna under test (AUT) in the anechoic chamber.
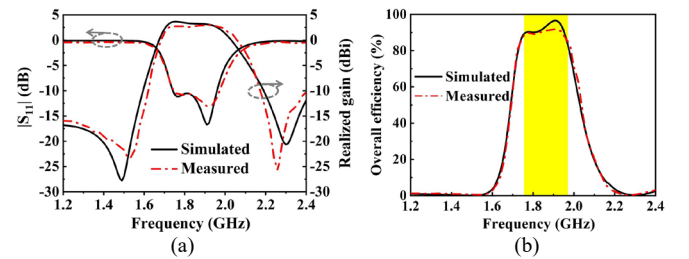
Fig. 7. Simulated and measured results of the optimized omnidirectional filtenna. (a) |S$_{11}$| and realized gain. (b) Overall efficiency. The measured operational –10 dB impedance band is highlighted in yellow.

The simulated and measured |S$_{11}$|, realized gain and overall efficiency values of the developed omnidirectional, electrically small, VP, top-hat loaded monopole-based filtenna are presented in Fig. 7. As presented in Fig. 7(a), the measured (simulated) –10 dB impedance bandwidth is from 1.76 to 1.97 GHz (1.74 to 1.96 GHz), i.e., 11.3% (11.9%) FBW. It also demonstrates that the measured (simulated) realized gain curve exhibits a very good filtering

response with a sharp roll-off at both of its band edges. Two radiation nulls were located at 1.52 GHz (1.49 GHz) and 2.28 GHz (2.3 GHz), respectively. Moreover, the measured (simulated) overall efficiency values within the entire operational bandwidth are higher than 83% (85%) as shown in Fig. 7(b). In general, the measured results agree well with their simulated values.

The simulated and measured normalized realized gain patterns in the two principal planes are shown in Fig. 8 at the center frequency, 1.85 GHz. It is clearly seen that the *H*-plane pattern in Fig. 8(b) is omnidirectional. The measured co-polarized fields were at least 14 dB stronger than their cross-polarized counterparts. The measured results are again in good agreement with their simulated values. Note that the asymmetry of the *E*-plane pattern is caused by the introduction of the shorting post. The significant currents on it increase the far-field radiation levels on its side. Other post positions remove the asymmetry but at the cost of smaller bandwidths.

Fig. 8. Simulated and measured normalized realized gain patterns of the optimized prototype of the omnidirectional, electrically small, VP filtenna operating at 1.85 GHz. (a) *E*-plane ($\varphi = 270°$). (b) *H*-plane ($\theta = 50°$).

III. ENDFIRE RADIATING, VP, ELECTRICALLY SMALL FILTENNA

It has been found that the two hybrid quarter-wavelength open-end stubs and shorting post augmentation of the top-hat monopole antenna has general applicability to other antennas. In the same manner as the developed omnidirectional system, they enable other types of filtennas to achieve radiation nulls at their band-edges that improve their out-of-band filtering performance, as well as providing the means to control the appearance of the resonance associated with them to enhance the system's impedance bandwidth while maintaining its electrically small size and radiation pattern behavior over the entire operational bandwidth. To demonstrate further the importance of this innovative approach, an endfire radiating, electrically small, VP filtenna was developed.

Its configuration is detailed in Fig. 9. The electrically small filtenna design consists of a driven fan-shaped top-loaded folded monopole element and a fan-shaped top-loaded monopole near-field resonant parasitic (NFRP) element. Each of the fan-shaped components includes a meander-slot on the top layer of the upper substrate. These design choices ensure the compactness of the entire system. The basic concept of this design was inspired by the electrically small NFRP antenna developed in [14].

As is detailed in Fig. 9(a), it includes two layers of dielectric substrates, three copper posts, and a metal ground plane. The substrates are again the Rogers RO4003. They are circular disks with a radius of 21.0 mm and a thickness of 0.813 mm. The bottom surface of the lower substrate is directly connected to the circular ground plane which has a radius of 150.0 mm and a thickness of 1.0 mm. Two quarter-wavelength open-end stubs with different lengths are etched on the top surface of the lower substrate and oriented in parallel with a gap, $g = 0.2$ mm, between them. The shorter Stub 1 has a dimension $L_{s1} \times W_{s1}$. Because of the presence of the NFRP element, the top half-axe was not necessary for impedance tuning.

The longer Stub 2 with its top half-axe shape has a rectangular slot with the dimensions $L_4 \times W_4$ etched into it. The ends of the two shorting posts are, respectively, connected to the metal sectors that constitute the top hat and to the ground plane. The inner conductor of the coax feed is connected to the two stubs and directly to the driven post. A 50 Ω SMA connector is again adopted to feed the antenna. The optimized design parameters are given in Table II.
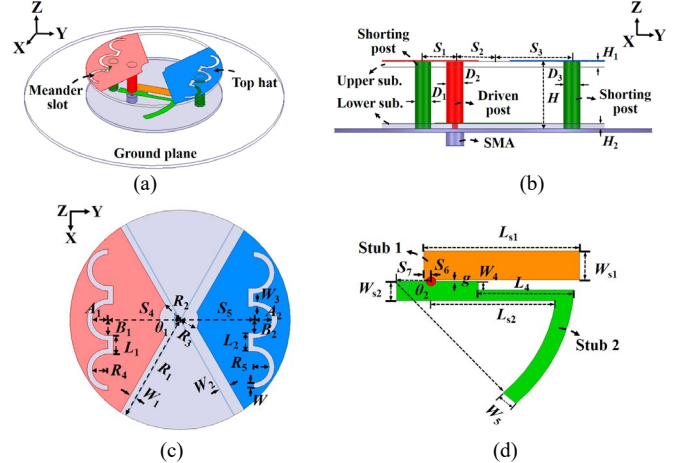
Fig. 9. The configuration and design parameters of the endfire-radiating, electrically small, VP filtenna. (a) 3-D isometric view. (b) Side view. (c) Top view of the top hats. (d) Top view of the stubs.

TABLE II OPTIMIZED DESIGN PARAMETERS OF THE ENDFIRE RADIATING, VP, ELECTRICALLY SMALL FILTENNA (IN MILLIMETERS)

$S_1 = 6.0$	$S_2 = 7.2$	$S_3 = 14.8$	$H_1 = 0.813$	$H_2 = 0.813$
$D_1 = 2.6$	$D_2 = 3.2$	$D_3 = 4.4$	$S_4 = 13.75$	$S_5 = 14.0$
$R_1 = 21.0$	$R_2 = 4.0$	$R_3 = 3.5$	$R_4 = 3.0$	$R_5 = 3.0$
$L_1 = 3.5$	$L_2 = 3.5$	$W = 1.0$	$W_1 = 1.0$	$W_2 = 2.0$
$W_3 = 0.85$	$A_1 = 4.0$	$B_1 = 4.0$	$A_2 = 3.445$	$B_2 = 2.65$
$L_{s1} = 17.2$	$W_{s1} = 3.4$	$L_{s2} = 17.7$	$W_{s2} = 2.3$	$L_4 = 10.7$
$W_4 = 1.0$	$W_5 = 1.9$	$S_6 = 0.8$	$S_7 = 3.8$	$H = 8.37$
$g = 0.2$	$\theta_1 = 120°$	$\theta_2 = 41°$	None	

A. Simulated and Measured Results

The endfire-radiating, VP filtenna was also experimentally tested. Its prototype's pieces before assembly are shown in Fig. 10(a). The test equipment and measurement environment are the same to those shown in Fig. 6. The AUT is shown in Fig. 10(b).
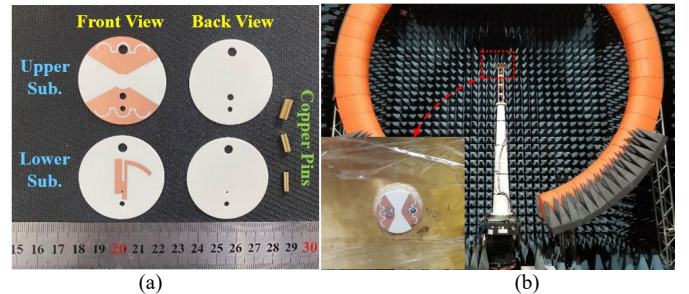
Fig. 10. Fabricated endfire-radiating, VP filtenna. (a) Front and back views of each layer before assembly. (b) AUT in the anechoic chamber.

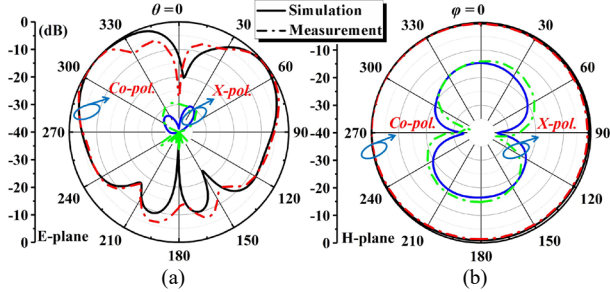The simulated and measured |S11|, realized gain, and overall efficiency values of the endfire-radiating VP filtenna are presented in Fig. 11. The simulated –10 dB FBW is 13.7% (1.91–2.19 GHz) and its measured value is 12.8% (1.9–2.16 GHz). The two radiation nulls introduced by the stub-post assemblage are located at 1.84 and 2.5 GHz. As shown in Fig. 11(b), the simulated overall efficiency values

are greater than 80% over the entire passband, from 1.91 to 2.19 GHz. The measured values are over 78%. A good frequency filter response with fast roll-offs at the band edges is observed in the measured realized gain curve. Additionally, there are slight discrepancies between the simulated and measured results. Additional tolerance simulations allow us to attribute them to small errors that occurred in the fabrication and measurement processes. In general, the measured results are in good agreement with their simulated values.
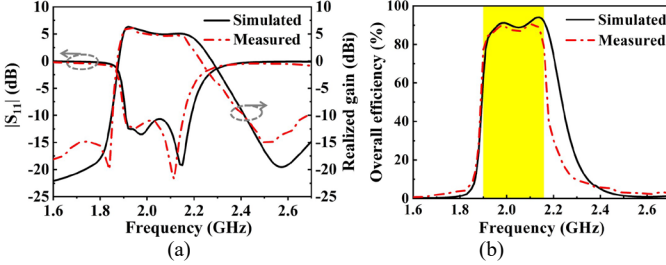

Fig. 11. Simulated and measured results of the optimized endfire radiating, VP filtenna. (a) $|S_{11}|$ and realized gain. (b) Overall efficiency. The measured operational –10 dB impedance band is highlighted in yellow.

The simulated and measured 2D normalized radiation patterns in the two principal planes and simulated 3D pattern are given in Fig. 12 at the center frequency of the operating band, 2.05 GHz. It is noted in Fig. 12(a) that the offset of the driven element and the relatively large ground plane make the main beam in the E-plane (yz plane) point not along the ground plane, but above it at the angle ~50°. This is a common effect experienced with a VP monopole on a large, but finite ground plane as discussed in [3], [5], [15], [16]. The H-plane results shown in Fig. 12(b) illustrate the endfire radiation characteristic of the system. Nevertheless, the measured co-polarized fields are at least 17 dB stronger than their cross-polarized counterparts within the ± 60° sector, and more in the remaining 240º range. The 3D realized gain pattern is also presented in Fig. 12(c) for easy observation.
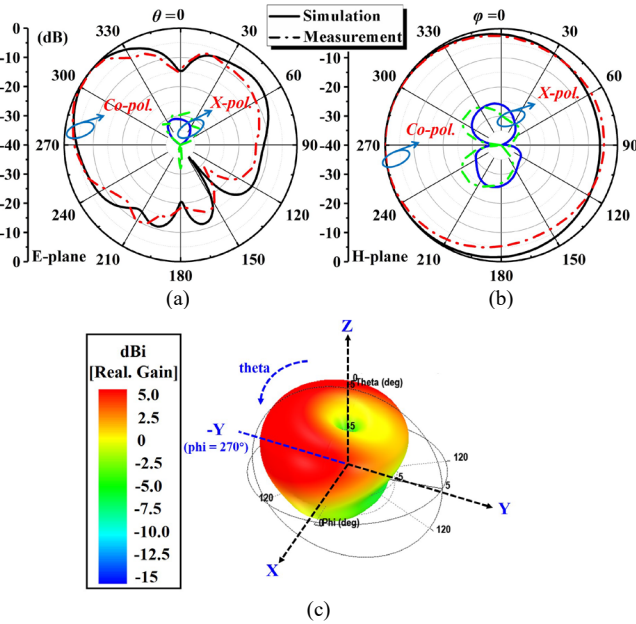

Fig. 12. Simulated and measured 2D normalized realized gain patterns and simulated 3D realized gain pattern of the prototype endfire-radiating, electrically small, VP filtenna at its center frequency, 2.05 GHz. (a) E-plane (φ =270°). (b) H-plane (θ = 50°). (c) Simulated 3D realized gain pattern.

B. Operating mechanisms

The operating mechanisms of the end-fire system were investigated by studying the surface current distributions on its metallic components. The current distributions at the two out-of-band radiation nulls, 1.8 and 2.57 GHz, on the posts and on the metallic sectors of the top-hats at the two radiation nulls are very weak. This feature is analogous to what was found in the omnidirectional system. Similarly, the current distributions are strongly concentrated on the resonant longer and shorter quarter-wavelength open-end stubs at the lower and higher null frequencies, respectively.

The surface current distributions at the first two resonance frequencies, 1.92 and 1.98 GHz, on the posts and top-hats are stronger than those at the third resonance frequency, 2.15 GHz. The currents on the posts are vertically polarized, and those on the top-hat sectors are concentrated near the meander slots. These resonant sectors and the driven post establish a quasi-Yagi mode [17], [18] in which the left sector acts as the director, the post is driven element, and the right sector acts as the reflector element. The presence of the resonant slots in the sectors leads a significant red-shift of the resonance frequencies, which facilitates the overall system being electrically small. The current distributions at the third resonance frequency, 2.15 GHz, are noticeably stronger on the stubs than the ones on the top-hat and posts. This feature confirms that the third resonance is introduced by the half-wavelength resonator composed of the two open-end stubs. While the currents on Stub 1 and Stub 2 are parallel, they are oriented in the opposite direction and have nearly the same magnitude. This behavior leads to a difference pattern in the broadside direction. Consequently, the antenna radiates primarily an endfire-like radiation pattern with VP fields that arise from the currents on the posts and slotted sectors in the same manner as those present at the first two resonances.

TABLE III
COMPARISON OF THE PERFORMANCE CHARACTERISTICS OF THE DEVELOPED FILTENNAS WITH RELATED FILTENNAS REPORTED IN THE LITERATURE

Refs.	$ka_{radiator}$	FBW (%)	R.G. (dBi)	Num. of RN	Pattern	Pol.
[10]	1.31	52.8	0.84	2	Omni.	VP
[19]	1.89	6.3	6.73	0	Broadside	HP
[20]	2.05	14	0.65	1	Omni.	HP
[21]	1.31	14.9*	8	2	Broadside	HP
[22]	1.95	8.67	7.2	2	Broadside	HP
[23]	1.98	19.6	10.4	3	Broadside	HP
[24]	3.43	28.4	8.2	2	Broadside	HP
[25]	3	20.3	9.05	2	Broadside	HP
[26]	1.17	12.2*	9.4	2	Broadside	HP
[27]	0.87	1	4.8	2	Broadside	HP
This work	0.73	11.3	3.01	2	Omni.	VP
	0.93	12.8	6.09	2	Endfire	VP

*:$|S_{11}| < $-15 dB. R.G.: realized gain. RN: radiation null. Pol.: polarization.

IV. PERFORMANCE COMPARISONS

The performance characteristics of our developed omnidirectional-radiating and endfire-radiating VP filtennas are compared to those of recently reported filtennas in Table III. In order to make fair comparisons, the total electrical size of each design corresponds to the lowest frequency of its -10 dB impedance bandwidth. Several of the comparison filtennas use the antenna's radiator as a replacement for the last-stage resonator of a filter [19], [20]. However, the overall sizes of these antennas are large. Moreover, the insertion loss caused by their filtering mechanisms is inevitably large as well. As a consequence, their gains are reduced. In contrast, our systems are electrically small and their filtering aspects do not impact their realized gain performance. On the other hand,

several of the designs use stacked structures [21]-[23] and custom-designed feed structures [24]-[26] to obtain their desirable filtering responses. As a result, their entire volumes are also unavoidably large and electrically large with $ka_{radiator} > 1$.

As Table III also indicates, previous studies mainly focused on HP filtenna designs. Even though the dense dielectric patch (DDP) of the HP filtering antenna in [27] is electrically small with $ka_{radiator} = 0.87$, its 1.0% FBW is narrow and is less than *one-tenth* of the value attained by our systems. Furthermore, the sizes of our developed VP filtennas are much electrically smaller when compared with the VP dielectric resonator filtenna successfully realized in [10]. Moreover, they hold relatively higher realized gain values throughout their operating bandwidths.

V. CONCLUSION

Vertically polarized, electrically small, filtennas with omnidirectional and endfire radiation performance were developed in this paper. The evolution of the omnidirectional system from a monopole to a top-hat monopole antenna loaded with two quarter-wavelength open-end stubs and a shorting post was provided to illustrate the operating mechanisms of its final design. The lower-band and upper-band radiation nulls in both filtenna designs were generated by the quarter-wavelength open-end stubs, their lengths being different. These nulls facilitate the sharp roll-off rate at both of those band-edges. Moreover, it was demonstrated the frequency of each radiation null can be adjusted individually. It was also demonstrated that the additional in-band resonance produced by the two stubs effectively enhances the bandwidths of both antennas without impacting their monopole radiation performance.

The optimized prototypes were fabricated, assembled, and tested. The measured results, in good agreement with their simulated values, demonstrated that the omnidirectional and endfire vertically polarized filtennas, respectively, exhibit FBWs of 11.3% and 12.8%, even though both are electrically small in size. Comparisons with previously reported filtennas illustrated their advantages, notably their vertically polarized fields and their electrically small sizes. Their performance characteristics make these VP filtennas particularly interesting for many potential applications in current and future space-limited wireless systems. Examples include mobile and indoor wireless communications [10], long distance communications [28] and automotive radar systems [29].

REFERENCES

[1] W. Hong and K. Sarabandi, "Low profile miniaturized planar antenna with omnidirectional vertically polarized radiation," *IEEE Trans. Antennas Propag.*, vol. 56, no. 6, Jun. pp. 1533–1540, 2008.

[2] J. Liu and Q. Xue, "Microstrip magnetic dipole Yagi array antenna with endfire radiation and vertical polarization," *IEEE Trans. Antennas Propag.*, vol. 61, no. 3, pp. 1140–1147, Mar. 2013.

[3] R. Wang, B.-Z. Wang, G.-F. Gao, X. Ding, and Z.-P. Wang, "Low-profile pattern-reconfigurable vertically polarized endfire antenna with magnetic-current radiators," *IEEE Antennas Wireless Propag. Lett.*, vol. 17, no. 5, pp. 829–832, May 2018.

[4] L. Sun, Y. Hou, Y. Li, Z. Zhang, and Z. Feng, "An open cavity leaky-wave antenna with vertical-polarization endfire radiation," *IEEE Trans. Antennas Propag.*, vol. 67, no. 5, pp. 3455–3460, May 2019.

[5] H. Tian, L. Jiang, and T. Itoh, "Compact endfire coupled-mode patch antenna with vertical polarization," *IEEE Trans. Antennas Propag.*, vol. 67, no. 9, pp. 5885–5891, Sep. 2019.

[6] J. Oh and K. Sarabandi, "Low profile vertically polarized omnidirectional wideband antenna with capacitively coupled parasitic elements," *IEEE Trans. Antennas Propag.*, vol. 62, no. 2, pp. 977–982, Feb. 2014.

[7] X. Chen, K. Huang, and X.-B. Xu, "A novel planar slot array antenna with omnidirectional pattern," *IEEE Trans. Antennas Propag.*, vol. 59, no. 12, pp. 4853–4857, Dec. 2011.

[8] R. Wang, B.-Z. Wang, and X. Ding, "Broadband quasi-bidirectional antenna with vertical polarization," *IEEE Antennas Wireless Propag. Lett.*, vol. 17, no. 12, pp. 2232–2236, Dec. 2018.

[9] A. T. Mobashsher, A. J. Pretorius, and A. M. Abbosh, "Low-profile vertical polarized slotted antenna for on-road RFID-enabled intelligent parking," *IEEE Trans. Antennas Propag.*, vol. 68, no. 1, pp. 527–532, Jan. 2020.

[10] P. F. Hu, Y. M. Pan, K. W. Leung, and X. Y. Zhang, "Wide-/dual-band omnidirectional filtering dielectric resonator antennas," *IEEE Trans. Antennas Propag.*, vol. 66, no. 5, pp. 2622–2627, May 2018.

[11] M.-C. Tang and R. W. Ziolkowski, "A study of low–profile, broadside radiation, efficient, electrically small antennas based on complementary split ring resonators," *IEEE Trans. Antennas Propag.*, vol. 61, no. 9, pp. 4419–4430, Sep. 2013.

[12] D. M. Pozar, *Microwave Engineering*. New York, NY, USA: Wiley, 2005.

[13] SG128 multi-probe antenna measurement system. [Online]. Available: https://www.mvg-world.com/en/system/files/datasheet_sg128_bd.pdf

[14] M.-C. Tang, Y. Duan, Z. Wu, X. Chen, M. Li, and R. W. Ziolkowski, "Pattern reconfigurable, vertically polarized, low-profile, compact, near-field resonant parasitic antenna," *IEEE Trans. Antennas Propag.*, vol. 67, no. 3, pp. 1467–1475, Mar. 2019.

[15] Z. Hu, W. Wang, Z. Shen, and W. Wu, "Low-profile helical quasi-Yagi antenna array with multibeams at the endfire direction," *IEEE Antennas Wireless Propag. Lett.*, vol. 16, pp. 1241-1244, 2017.

[16] Y. Zhao, Z. Shen, and W. Wu, "Wideband and low-profile monocone quasi-Yagi antenna for endfire radiation," *IEEE Antennas Wireless Propag. Lett.*, vol. 16, pp. 325-328, 2017.

[17] M.-C. Tang, B. Zhou, Y. Duan, X. Chen, and R. W. Ziolkowski, "Pattern-reconfigurable, flexible, wideband, directive, electrically small near-field resonant parasitic antenna," *IEEE Trans. Antennas Propag.*, vol. 66, no. 5, pp. 2271–2280, May 2018.

[18] M.-C. Tang, B. Zhou, and R. W. Ziolkowski, "Flexible uniplanar electrically small directive antenna empowered by a modified CPW-feed," *IEEE Antennas Wireless Propag. Lett.*, vol. 15, pp. 914–917, 2016.

[19] K.-Z. Hu, M.-C. Tang, Mei Li, and Richard W. Ziolkowski, "Compact, low-profile, bandwidth-enhanced substrate integrated waveguide filtenna," *IEEE Antennas Wireless Propag. Lett.*, vol. 17, no. 8, pp. 1552–1556, Aug. 2018.

[20] C.-T. Chuang and S.-J. Chung, "Synthesis and design of a new printed filtering antenna," *IEEE Trans. Antennas Propag.*, vol. 59, no. 3, pp. 1036–1042, Mar. 2011.

[21] Y. Zhang, X. Y. Zhang, L.-H. Ye, and Y.-M. Pan, "Dual-band base station array using filtering antenna elements for mutual coupling suppression," *IEEE Trans. Antennas Propag.*, vol. 64, no. 8, pp. 3423–3430, Aug. 2016.

[22] K. Xu, J. Shi, X. Qing, and Z. N. Chen, "A substrate integrated cavity backed filtering slot antenna stacked with a patch for frequency selectivity enhancement," *IEEE Antennas Wireless Propag. Lett.*, vol. 17, no. 10, pp. 1910–1914, Oct. 2018.

[23] X. Y. Zhang, W. Duan, and Y.-M. Pan, "High-gain filtering patch antenna without extra circuit," *IEEE Trans. Antennas Propag.*, vol. 63, no. 12, pp. 5883–5888, Dec. 2015.

[24] Y. M. Pan, P. F. Hu, X. Y. Zhang, and S. Y. Zheng, "A low-profile high-gain and wideband filtering antenna with metasurface," *IEEE Trans. Antennas Propag.*, vol. 64, no. 5, pp. 2010–2016, May 2016.

[25] P. F. Hu, Y. M. Pan, X. Y. Zhang, and S. Y. Zheng, "A compact filtering dielectric resonator antenna with wide bandwidth and high gain," *IEEE Trans. Antennas Propag.*, vol. 64, no. 8, pp. 3645–3651, Aug. 2016.

[26] W. Duan, X. Y. Zhang, Y.-M. Pan, J.-Xu Xu, and Q. Xue, "Dual-polarized filtering antenna with high selectivity and low cross polarization," *IEEE Trans. Antennas Propag.*, vol. 64, no. 10, pp. 4188–4196, Oct. 2016.

[27] X.-Y. Wang, S.-C. Tang, X.-F. Shi, and J.-X. Chen, "A low-profile filtering antenna using slotted dense dielectric patch," *IEEE Antennas Wireless Propag. Lett.*, vol. 18, no. 3, pp. 502–506, Mar. 2019.

[28] Z. Liang, Y. Li, J. Liu, S. Y. Zheng, and Y. Long, "Microstrip magnetic monopole endfire array antenna with vertical polarization," *IEEE Trans. Antennas Propag.*, vol. 64, no. 10, pp. 4208–4217, Oct. 2016.

[29] Y. He, K. Ma, N. Yan, Y. Wang, and H. Zhang, "A cavity-backed endfire dipole antenna array using substrate-integrated suspended line technology for 24 GHz band applications," *IEEE Trans. Antennas Propag.*, vol. 66, no. 9, pp. 4678–4686, Sep. 2018.